Static and dynamic precipitation phenomena in laser powder bed-fused Ti6Al4V alloy

Emanuela Cerri [a], Emanuele Ghio [a,*], Stefano Spigarelli [b], Marcello Cabibbo [b], Giovanni Bolelli [c,d,e]

[a] *Department of Engineering and Architecture, University of Parma, Via G. Usberti 181/A, 43124, Italy*
[b] *DIISM, Università Politecnica delle Marche, Via Breccie Bianche 12, 60131, Italy*
[c] *Department of Engineering "Enzo Ferrari", University of Modena e Reggio Emilia, Via P. Vivarelli 10/1, 41125, Italy*
[d] *InterMech – MO.RE. Centro Interdipartimentale per la Ricerca Applicata e i Servizi nel Settore della Meccanica Avanzata e della Motoristica, Università di Modena e Reggio Emilia, Via Pietro Vivarelli 2, 41125, Modena, Italy*
[e] *Consorzio Interuniversitario Nazionale per la Scienza e Tecnologia dei Materiali (INSTM), Local Unit: Università di Modena e Reggio Emilia, Via Pietro Vivarelli 10/1, 41125, Modena, Italy*

ARTICLE INFO

ABSTRACT

The present paper investigates static and dynamic precipitation phenomena in the Ti6Al4V alloy produced via laser-powder bed fusion, solubilized at 1050 °C and aged in the range of 450–650 °C. In relation to the distance from the platform on which the samples are disposed during the solution heat treatment, the microstructure varies from α-laths to α-colonies arranged in a Widmanstätten structure. The aging heat treatment at 450 °C promotes the formation of stacking faults into α-laths and the precipitation of α_2-Ti$_3$Al phases. SEM and TEM observations reveal that the density of precipitates increases after aging at 500 °C, while coarsening of the α-phase occurs only after aging heat treatment at 600 °C. Vickers microhardness measurements reveal different peak-aging conditions and show that the alloy is unstable at high temperatures (T > 450 °C), both in the case of static and dynamic precipitation phenomena. Only the aging profile at 450 °C shows a constant trend of Vickers microhardness after 4 h of treatment.

1. Introduction

The Ti6Al4V alloy is widely used for aerospace, automotive, and biomedical applications due to its perfect combination of high hardness and tensile strength at room and elevated temperatures, corrosion resistance, toughness, and density ($\sim$4.5 g/cm^3) [1–3]. Ti6Al4V is an α/β titanium alloy showing an α+β microstructure at room temperature thanks to the α- (e.g., Al, O, and C) and β-stabilizer (e.g., V, Fe) alloying elements. In relation to the several production processes and postprocess heat treatments, the α-phase may form the following types of microstructures: i) acicular martensite, ii) lath or iii) colonies in the Widmanstätten or basketweave structure, and iv) duplex or bimodal structure in which the primary α-phase (untransformed) is combined with the secondary α-phase (transformed by the β-phase) [4–8]. The β-phase precipitates, instead, along the grain boundaries of the α-phase due to the diffusion-based process of the β-stabilizer alloying elements.

Laser powder bed-fused Ti6Al4V alloy produced by L-PBF shows a fully martensitic microstructure contained in columnar β-grains that are arranged parallel to the build direction [1,8,9]. The β → α′-martensite diffusionless transformation is promoted by the high cooling rate ($\sim$10^7 K/s) characterizing the solidification process of the molten pool during which the β-stabilizer elements become trapped within the hexagonal close-packed (hcp) lattice structure of the α-phase. Yang et al. [8] showed that the martensitic microstructure is a hierarchical structure including primary, secondary, tertiary, and quartic α′-martensite laths, which are placed perpendicular to each other. These acicular sharp α′-martensite phases are associated with high ultimate tensile ($\geq$ 1.1 GPa, [1,10]) and yield strengths ($\geq$ 1 GPa, [1,10]) but low ductility (< 10%, [1]), which makes α′-martensite undesirable for many applications in aerospace and automotive fields. In relation to the process parameters used to additively manufactured Ti6Al4V samples and, consequently, to the obtained microstructure morphology Vickers microhardness can

---

Table 1

Chemical composition (wt. %) of Ti6Al4V-ELI powder.

Ti	Al	V	Fe	O	N	H	C
Balance	6.47	4.06	0.21	0.09	0.01	0.001	0.01

vary from (364 ± 27) HV0.2 to (420 ± 10) HV0.2 [11–14]. Vanadium β-stabilizer atoms are contained in the hcp lattice, and due to their cytotoxicity, α'-martensite must be avoided in medical implants [15]. As-built Ti6Al4V samples are also characterized by high residual stresses due to the rapid heating and cooling cycles developed during the powder bed process [8,16]. At the same time, this complex thermal history may promote the precipitation of intermetallic phases, such as α_2-Ti$_3$Al and/or TiAl$_3$, when the temperature reaches 500–600 °C [12,17]. This condition improves the ultimate tensile strength, yield strength, and hardness, as investigated by Refs. [18,19].

In this scenario, postprocess heat treatments and cooling methods (rates) are required to relieve the residual stress, decompose the α'-martensite and generate the appropriate mechanical properties and microstructure. Ali et al. [20] showed that α'-martensite decomposition into an α+β microstructure can already be obtained at 470 °C. Kaschel et al. [21] affirmed that α'-martensite decomposes at temperatures higher than 400 °C given that a variation in the hcp lattice parameters is detected. A complete decomposition process, in which the α-phase preserves the crystallographic orientation of the α'-martensite laths, can be generally obtained at temperatures in the range of 700–800 °C [4, 22–24]. Moreover, annealing in the range of 700–900 °C relieves residual stress and α-phase grain growth and does not promote precipitation phenomena [25,26]. In this scenario, the ultimate tensile and yield strengths of Ti6Al4V samples decrease from ~1.1 GPa to ~950 MPa and from ~1 GPa to ~850 MPa, respectively. Wu et al. [13] measured an increment of ~27 HV0.2/100 °C after annealing heat treatments in the range 300–500 °C due to the structure refinement. Vickers measurements decrease only considering samples annealed above 600 °C. Previous studies [27,28] have measured HV values of 350 ± 26 HV0.1 (after 700 °C x 1 h) or 295 HV0.2 (after 850 °C x 2 h). On the other hand, Ti6Al4V samples were characterized by 386 ± 9 HV0.5 and 321 ± 28 HV0.1 after 740 °C x 2 h and 900 °C x 2 h, respectively [4,27]. These differences were conferred by both the as-built microstructure that characterized the laser powder bed-fused Ti6Al4V alloy before the annealing HTs, and by the load used to measure the HV values [14]. Despite the occurrence of α'-martensite decomposition, ductility values are not improved significantly [1,10]. Otherwise, the solubilization heat treatment performed above the β-transus temperature has dual and better effects: i) the recrystallization of columnar β-grains into equiaxed ones that reduces the mechanical property anisotropy and ii) the control of the microstructure morphology (and thus the mechanical behavior) through the variation of heat treatment parameters [1,11]. The ultimate tensile and yield strength generally decrease to 870 MPa and 750 MPa, respectively [1,10]. The elongation values, however, increase with respect to the as-built values and generate a good combination with the tensile strengths. Vickers measurements vary instead in relation to the cooling method affecting Ti6Al4V samples after exposure at the solution temperatures. Wu et al. [13] showed (422 ± 3) HV0.2 after exposure at 1000 °C followed by water quenching, reaching the as-built HV measurements. Lekoadi et al. [11] revealed instead (344 ± 13) HV0.3 with an exposure temperature of 1000 °C for 2 h followed by furnace cooling. With the purpose of improving mechanical properties after a solution heat treatment, the present work investigates different aging HTs performed on Ti6Al4V samples manufactured by L-BPF, as the literature lacks this part. Lacks related to the effects promoted by aging HTs, performed in the range 450–650 °C, on laser powder bed-fused Ti6Al4V samples in terms of i) α_2-Ti$_3$Al precipitation phenomenon and ii) formation of micro and nanostructures in the α-laths. In detail, static and dynamic phenomena of precipitation, the microstructural morphologies of the α/β phases and their coarsening effects are investigated after both

solution and aging HTs to find the optimum HT conditions that confer the best mechanical properties. Vickers microhardness tests were used to understand these process-structure-properties.

2. Material and method/experimental procedure

Gas-atomized Ti6Al4V extra-low interstitial (ELI) powders, characterized by a diameter in the range from 15 to 60 μm, were used in this work. The powder chemical composition (Table 1) complies with the F1472 standard regulations to be an ELI alloy (wt.% of O < 0.13% and Fe < 0.25%).

Ti6Al4V dog-bone samples (Fig. 1a) were manufactured by the L-PBF process in an SLM®280 machine (SLM solutions, Lübeck, Germany) equipped with 400×2 W IPG fiber lasers by using a scanning speed of 1250 mm/s, a laser power of 340 W, a layer thickness of 60 μm and a hatch spacing of 120 μm. The build platform was preheated at 80 °C, and the build chamber was filled with argon gas to avoid powder oxidation processes. The building direction was parallel to the z-axis, as shown in Fig. 1a. 'Top' and 'Bottom' labels designate the farthest and closest regions to the build platform, respectively. After the manufacturing process, Ti6Al4V dog-bone samples were solution heat treated at 1050 °C for 1 h (Fig. 1b) in a vacuum furnace. These samples were not removed from the build platform for the SHT. The solution temperature at 1050 °C was reached by a furnace thermal ramp, with a first step at 600 °C × 1 h and a second step at 800 °C × 0.5 h. Subsequent aging was performed at 450°, 500° and 600 °C for times ranging from 1 to 128 h in a muffle furnace (Nabertherm GmbH, Lilienthal, Germany), followed by different cooling methods. The investigated cooling methods were i) water quenching (WQ), ii) air cooling (AC, ~5.5 °C/s) and iii) furnace cooling (FC, ~0.02 °C/s) (Fig. 1b, Table 2). Aging temperatures were chosen in relation to the temperature range in which Ti–Al may precipitate [26]. Dynamic precipitation phenomena were evaluated on crept samples, which were analyzed by Spigarelli et al. [22]. The present paper shows HV measurements obtained in the gauge length of the crept samples.

Static (S) and dynamic (D) age-hardening responses were evaluated through a Vickers microhardness test performed on grounded and polished sample surfaces (area of 10 × 15 mm^2 placed along the yz plane, Fig. 1a) using a load of 500 gf and an indentation time of 15 s in agreement with the UNI EN ISO 6507 standard. Each HV0.5 value shown in the present work was obtained by an average of 9 indentations arranged in a 3 × 3 matrix, as proposed in Ref. [29]. A Vickers microhardness test, with a load of 100 gf and an indentation time of 15 s, was also performed to evaluate the HV0.1 contribution conferred by the several microstructural morphologies revealed in solution-treated samples. For these reasons, HV0.1 values were measured after Keller's chemical etching (100 mL H$_2$O + 2 mL HF + 4 mL HNO$_3$).

Polishing was performed with a colloidal suspension for both Vickers measurements and microstructural analysis. Optical microscopy (OM) and scanning electron microscopy (SEM) observations were conducted using a DMi8 optical microscope (Leica, Wetzlar, Germany) equipped with image analysis software and a Nova NanoSEM 450 (Nova Nano-SEMTM, Oregon, USA) equipped with a field emission gun source, respectively. The phase composition was investigated by X-ray diffraction (XRD, X'Pert PRO, PANAlytical, Almeno, NL) using Cu-Kα radiation emitted from a source that operated at 40 mA and 40 kV.

For transmission electron microscopy (TEM) analyses, thin foils were extracted from crept sample heads. These were prepared by mechanical grinding and polishing to a typical thickness of 150 μm. This was followed by twin-jet electropolishing to reach 60 μm thickness using a Struers™ Tenupol-5® device (Struers Inc., Westlake, Cleveland, OH, USA) with a solution consisting of 5% perchloric acid, 35% butanol, and 60% methanol at −35 °C and voltage V = 24 V. TEM discs were dimpled down to a thickness of 60 μm and then ion-milled to electron transparency using a Gatan™ precision ion polishing system (Gatan Inc., Pleasanton, CA, USA) operating at 8 keV and under incident beam angle
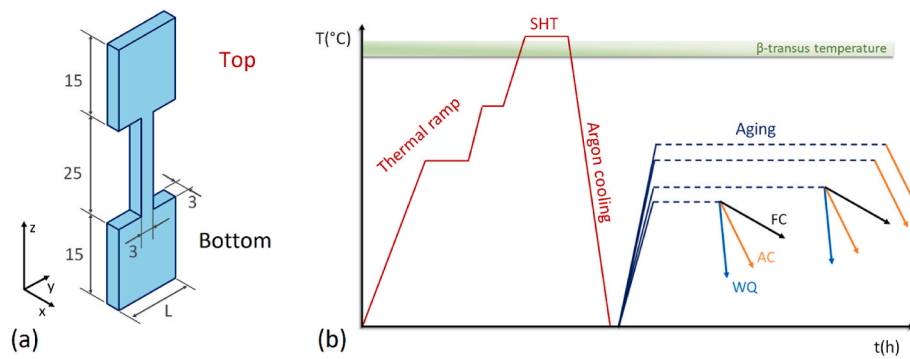
Fig. 1. (a) Geometry of manufactured Ti6Al4V samples where all measurements are expressed in millimetres and the z-axis represent the build direction; (b) Time-Temperature profiles representing the HTs performed on dog-bone Ti6Al4V samples. Blue dotted lines indicate the holding time range between 1 and 128 h. (For interpretation of the references to colour in this figure legend, the reader is referred to the Web version of this article.)

Table 2
Aging conditions.

Temperatures	Aging time [h]	Cooling method
450 °C	1, 2, 4, 8, 16, 32, 64, 128	WQ, AC, FC
500 °C		
600 °C		AC
650 °C		

of 8° and progressively reduced to 6° and 4°.

TEM inspections and analyses were performed using a Philips™ CM-20® microscope (Philips It, Milano, Italy) working at 200 kV and equipped with a double-tilt liquid nitrogen cooling specimen holder. Selected area diffraction patterns (SAEDPs) were recorded using a converged beam. Crystallography of the detected α, α', α_2 phases was analyzed by SAEDP acquired as having either α-[0001] or α-[2 $\overline{1}\overline{1}$0] parallel to the beam direction.

To quantify the microstructural features in solution-treated and aged samples, the α-phase thickness and equiaxed β-grain size were evaluated employing the methods recommended by Tiley et al. [30] and discussed by Li et al. [31], respectively. First, a grid composed of different lines of known lengths was overlaid on high-resolution SEM images. To reveal the closest size to the real thickness of the α-laths, the grid was rotated twice on the same SEM image due to the several orientations of the α-laths. The obtained number of intersections (λ) between the α-laths and the lines were used to calculate $\alpha_{thickness}$, as follows [30]:

$$\alpha_{thickness} = \left(\frac{1}{1.5(1/\lambda)_{mean}} \right) \tag{1a}$$

where 1.5 is a constant. Second, the equiaxed β-grain size was obtained

by counting the intersection between different lines, characterized by known lengths and causal orientations, and the grain boundaries. This system of lines was overlaid on maps formed by six OM micrographs taken at a magnification of 100X. In relation to the as-built conditions, in which columnar β-grains are arranged parallel to the build direction [1], the grain size was always obtained with the intersection method. In this case, the lines were drawn on OM micrographs at 200X and perpendicular to the samples' building direction (z-axis, Fig. 1a). The vol% of the β-phase and its dimensions were evaluated by image analysis software using binarized SEM micrographs.

3. Results

3.1. Microstructure

Fig. 2 shows the microstructure morphology of the as-built Ti6Al4V alloy in the xz- (Fig. 2a) and xy-planes (Fig. 2b). Columnar β-grains (width of 150 $\pm$ 30 μm) are arranged alongside the build direction and are entirely made up of α'-martensite laths (white arrow in Fig. 2a). They are formed thanks to the high cooling rate reached during the L-PBF process [1,32]. On the plane perpendicular to the build direction (xz plane in Fig. 2b), the quasisquare sections of the columnar β-grains are visible in the laser scan tracks, as discussed by authors in Ref. [4]. Cerri et al. [4] confirmed this arrangement through mathematically reconstructed EBSD maps measured on the same as-built samples. Fig. 2 also exhibits both lack-of-fusion (LOF) defects (Fig. 2a) and gas porosity (Fig. 2b) of different shapes [1,33]. The former defect is a void of irregular shape with its major axis of symmetry arranged parallel to the xy plane; the latter defect is characterized by the typical circular morphology. The relative density values of 99.57 $\pm$ 0.02% and 99.78 $\pm$ 0.01% for the Bottom and Top regions, respectively, define samples as
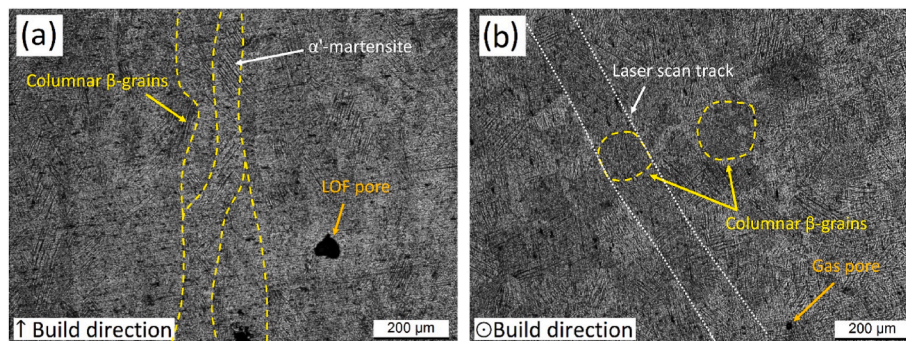

Fig. 2. OM micrographs of a Ti6Al4V sample in as-built conditions performed along the xz plane (a) and xy one (b). Yellow dotted lines and circles highlight the β-columnar grains that are analyzed in [4]. (For interpretation of the references to colour in this figure legend, the reader is referred to the Web version of this article.)
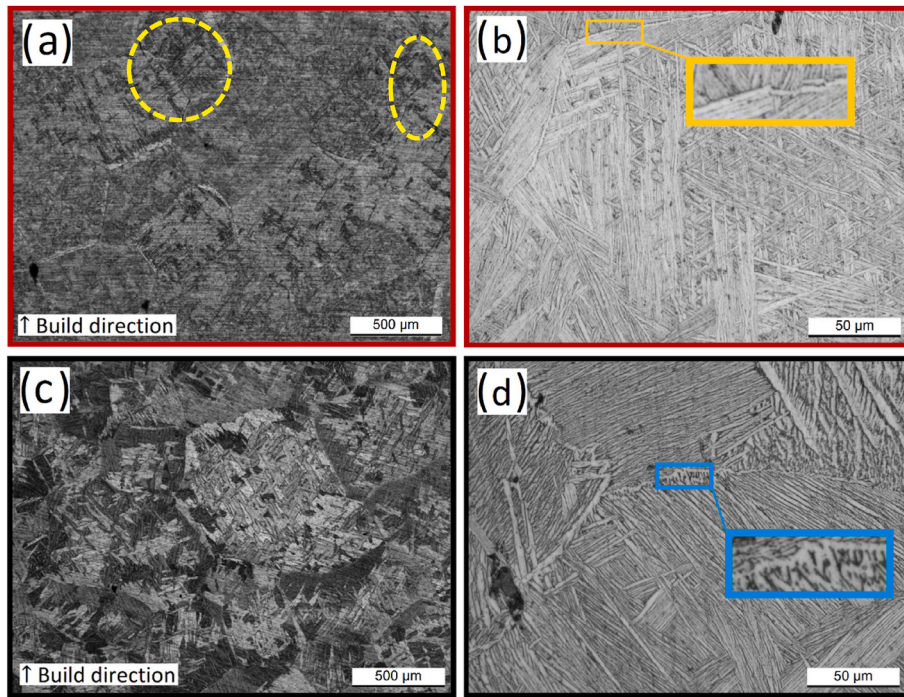
Fig. 3. OM micrographs of Top (a,b) and Bottom (c,d) regions of Ti6Al4V samples after SHT at 1050 °C × 1 h.
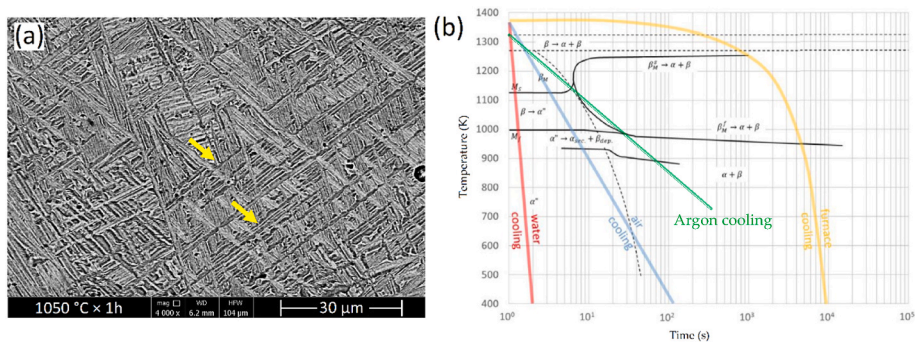

Fig. 4. α′-martensite laths, indicated by yellow arrows, that are formed into solubilized Ti6Al4V samples (a) due to the argon cooling pathway represented by the green line (b) (Adapted from Ref. [1]). (For interpretation of the references to colour in this figure legend, the reader is referred to the Web version of this article.)

fully dense and high-quality.

Fig. 3 shows the effects induced by the SHT at 1050 °C × 1 h, followed by argon cooling, on the microstructure of the Ti6Al4V samples at the Top and Bottom. Columnar β-grains recrystallized into equiaxed grains (Fig. 3a,c) on whose boundaries the α$_{GB}$ (Grain Boundary α) phase (Fig. 3b,d) is still present. During the β → α+β transformation, α+β colonies (Fig. 3c) nucleate and grow from the α$_{GB}$ toward the center of the grain, forming a Widmanstätten structure. Fig. 3c (Bottom sample) also shows both coarse α-laths and β-phase distributed along the α-grain boundary region due to the diffusion of the β-stabilizer alloying elements (V and Fe) from the center of the same α-laths toward their boundaries. The Top region instead shows an α+β Widmanstätten structure (Fig. 3b) mainly composed of α-laths rather than α-lamellar within the colonies thanks to a higher cooling rate that characterizes the farthest zone (Top) from the build platform. The same results are also supported by Ahmed et al. [34], who obtained similar microstructures with cooling rates of ~15 °C/s for the Top (Fig. 3a and b)and ~1.5 °C/s for the Bottom (Fig. 3c and d). The interconnection between the α$_{GB}$ and the α-laths/colonies (blue panel) and their separation through the β-phase (yellow panel) confirm the different cooling rates between the Bottom and the Top regions during the argon cooling [35]. As highlighted by the yellow

dotted ovals, the Top shows some needle-like α′-martensite, as confirmed by the TEM measurements performed on the same solubilized Ti6Al4V samples [22]. The same authors also found the same thickness for the α′-martensite laths and for the α-phase and their uniform distribution in the Widmanstätten structure. The same microstructure morphology of α′-martensite laths (Fig. 3a) is found in Ref. [36] after 1050 °C SHT and water quenching and in other studies [37,38].

The presence of needle-like α′-martensite in the SHT samples is also revealed through SEM observations (Fig. 4a). In fact, the argon cooling path intersects the M$_s$ (Martensite Start) line shown in the CCT diagram of Fig. 4b, which confirms the presence of an α′+α+β microstructure at room temperature due to the cooling rate of approximately 4.5 °C/s. The same microstructure morphology was presented by Rousseau et al. [39], who defined it as partially decomposed α′-martensite, and by Ref. [40], in which the same authors showed an α+α′(α'')$_{trace}$+β microstructure after cooling from 1050 °C at a rate of 3.5 °C s^{-1}. Sieniawski et al. [40] affirmed that a morphology such as Fig. 3d is obtained after cooling from 1050 °C at a rate <2 °C/s. In this scenario, the Bottom region can be characterized by a lower cooling rate than the Top region, as also previously discussed, due to the thermal inertia of the build platform.

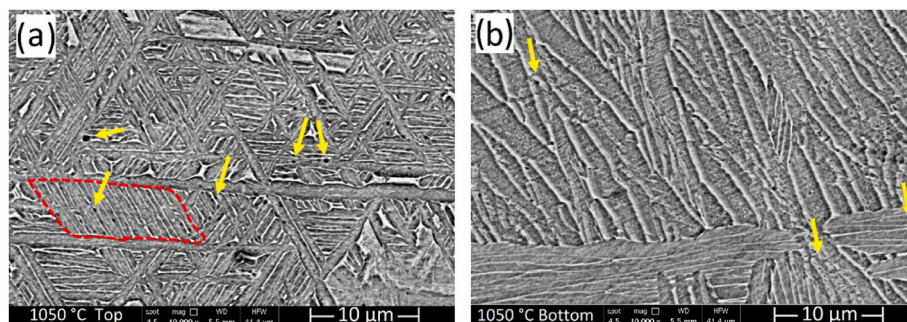Fig. 5 illustrates SEM micrographs of the Top (Fig. 5a) and Bottom

Fig. 5. SEM micrographs of Top (a) and Bottom (b) regions of a Ti6Al4V sample after SHT at 1050 °C. Yellow arrows indicate black blocky of precipitation and red dotted line highlights the presence of a α-colony. (For interpretation of the references to colour in this figure legend, the reader is referred to the Web version of this article.)

Table 3
EDX spectra (wt.%) of the lighter and darker zones shown in Fig. 5.

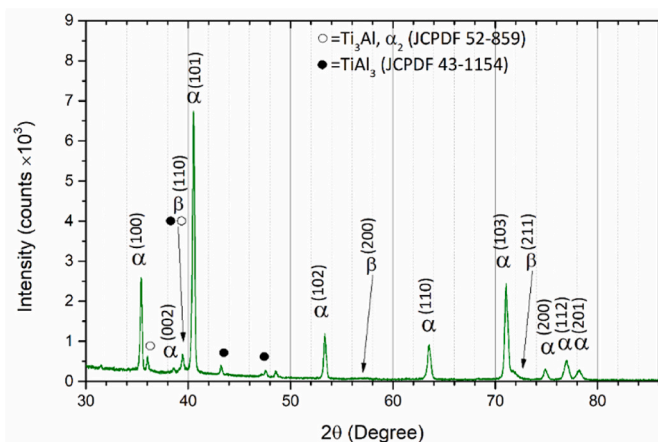| Spectra	Ti	Al	V	Fe	Phase
Darker zone	91.64	7.38	0.98	–	α
Lighter zone	90.75	0.89	8.21	0.15	β

Fig. 6. XRD spectrum of Ti6Al4V sample solubilized at 1050 °C per 1 h.

(Fig. 5b) regions; the α-phase is darker due to the α-stabilizer elements (Al, O, C), while β is lighter because of V and Fe (β-stabilizers), as confirmed by the EDX spectra listed in Table 3.

Fig. 5a shows the α+β Widmanstätten structure with the α-laths (Fig. 3c) rotated by 60° one to each other and delimitating some areas where α+β colonies are present (red dotted line). Fig. 5b confirms the presence of α+β Widmanstätten colonies at the Bottom. Both SEM micrographs show the presence of black blocky features (indicated by yellow arrows), which, according to the XRD spectrum (Fig. 6), may be identified as α_2-Ti$_3$Al and TiAl$_3$ intermetallic phases [1,22,41]. Both intermetallics may have formed, first, during the L-PBF process due to different thermal peaks developed by the laser source into the melt powder bed and, second, during the thermal ramp of the SHT (Fig. 1b) [1,22,41].

The difference in cooling rates between the Top and Bottom produced slightly coarser α-laths at the Bottom (0.68 ± 0.03) μm than at the Top (0.54 ± 0.04) μm. The β-phase also showed a slight increase from (0.15 ± 0.02) μm to (0.17 ± 0.02) μm.

Fig. 7 shows the effects induced on the microstructure by aging HTs at 450 °C (Fig. 7a and b), 500 °C (Figs. 7c) and 600 °C (Fig. 7d) followed by air cooling (AC). In particular, the number of black blocky phases in Fig. 7a (450 °C-4 h) is similar to that in Fig. 7b (450 °C-8 h); despite the long aging time, the α-phase size remains essentially unaffected, varying

from (0.59 ± 0.05) μm to (0.62 ± 0.04) μm.

Coarsening effects of the black blocky precipitates are instead detectable at 500 °C (Fig. 7c); the β dimension (0.19 ± 0.02) μm and α-phase (0.62 ± 0.05) μm remain constant at the previously discussed values (Figs. 5 and 7a and b). Aging at 600 °C (Fig. 7d) promotes coarsening effects of black blocky phases and of both α- and β-phases up to (0.94 ± 0.06) μm and (0.23 ± 0.04) μm, respectively, as shown in Table 4. Finally, the size of the equiaxed β-grains was unaffected by the long exposure time at the aging temperatures (Table 4). Furnace cooling (FC) does not influence the dimensions of the α-phase, β-phase, and β-grains.

3.2. Vickers microhardness

Aging at 450 °C (Fig. 8a) promotes peak aging conditions after 4 h regardless of the cooling path. In this scenario, HV values increase by approximately 5–10% (Table 5) from the as-built to the peak-aging conditions due to the precipitation phenomena, and they remain almost constant up to 128 h (Fig. 7a and b).

Aging profiles at 500 °C (Fig. 8) do not show a real peak given that HV values remain constant at (362 ± 2) HV0.5. Considering that α- and β-phases do not show coarsening effects (Table 4), as well as β-grains, α′-martensite decomposition could balance the precipitation phenomena. In fact, the needle-like α′-martensite (Fig. 4a) can be transformed into the α-phase from 420 °C, as widely analyzed in Ref. [42]. Other authors show the same results at 450–500 °C [1,20]. Additionally, in this case, the WQ, AC, and FC paths do not affect the HV profiles. Fig. 8c shows the overlap between the aging profiles obtained at 450 °C, 500 °C and 600 °C in which all samples were air cooled. Furthermore, the aging HT at 600 °C does not significantly influence the HV measurements despite the precipitation phenomena in Fig. 7d. In this scenario, precipitates can continue to balance the worsening effects induced by α′-martensite decomposition on HV measurements and by the coarsening phenomena of the α- and β-phases. At 650 °C, no significant HV variation was revealed.

Dynamic precipitation of α-Ti$_3$Al that occurred in the crept sample gauge length at 500 °C (D-500 °C in Fig. 9) anticipates the aging peak shown in S-500 °C (Figs. 8 and 9) from 128 to 1 h. The D-600 °C microhardness curve shows a slight increase to 330 HV after 2–3 h of exposure with respect to the solubilized conditions (~350 HV0.5).

4. Discussion

4.1. Microstructure

The columnar β-grains, formed in the as-built microstructure of the Ti6Al4V sample, nucleate on the build platform during the scan of the first layer and then grow through each deposited and scanned layer (Fig. 2a). Several studies confirm that L-PBF technology promotes their
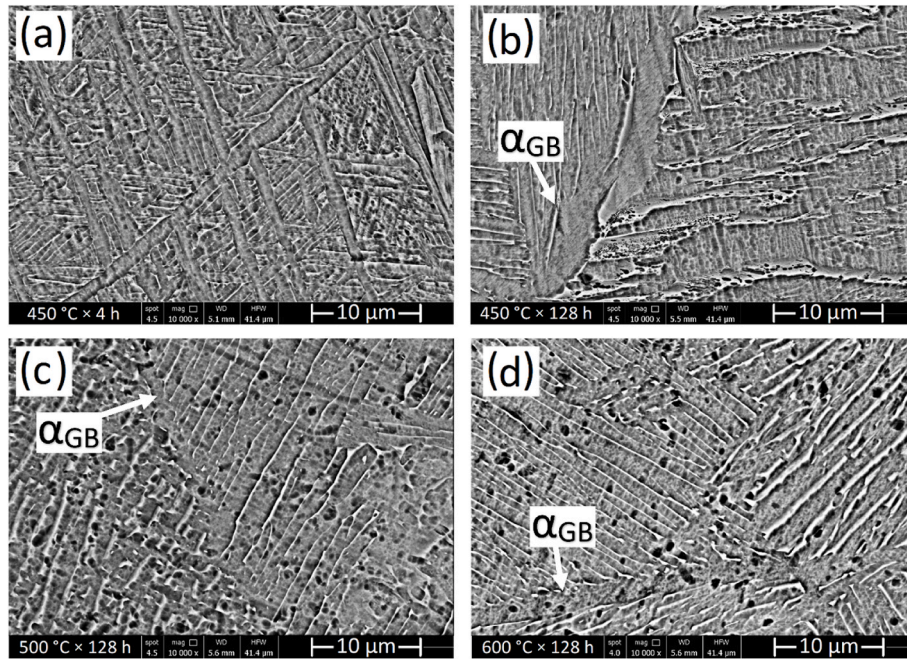
Fig. 7. Effects of aging HTs at 450 °C × 4 h (a), × 128 h (b), 500 °C × 128 h (c), and 600 °C × 128 h (d) on the microstructure of solubilized Ti6Al4V samples.

Table 4
Size in μm of α-phase, β-phase, and β-grain of Ti6Al4V after aging HT at 450 °C, 500 °C (AC), 500 °C (FC), and 600 °C per 128 h.

Size (μm) of	450 °C (AC)	500 °C (AC)	500 °C (FC)	600 °C (AC)
α-phase	0.62 ± 0.04	0.63 ± 0.05	0.61 ± 0.05	0.94 ± 0.06
β-phase	0.20 ± 0.02	0.19 ± 0.02	0.20 ± 0.02	0.23 ± 0.02
β-grain	360 ± 15	346 ± 16	350 ± 14	353 ± 18

columnar growth thanks to appropriate values of the G/R and G × R relationships, in which G is the thermal gradient [°K/s] and R is the solidification growth rate [m/s] [1,43]. Because the L-PBF technology is characterized by a high cooling rate (10^6–10^8 K/s, [1]), the β → α′-martensite transformation takes place during the cooling of the melt pool, so the columnar β-grains are full of needle-like α′-martensite that are disposed following a hierarchical structure [8]. It is basically formed by four different grades of α′-martensite, from primary to quartic, arranged perpendicular to each other. Primary α′-martensite extended into entire columnar β-grains with major axes several microns long. In fact, it nucleates on a boundary of the columnar β-grain and reaches the other side following an inclined direction of 45° (Fig. 2a). Secondary α′-martensite is characterized by smaller dimensions and is disposed perpendicular to the primary α′-martensite. Tertiary α′-martensite is generally found between the secondary laths, as well as finer quartic α′-martensite between the tertiary laths.

During a high-temperature SHT, namely, above the β-transus temperature, the columnar β-grains recrystallize into equiaxed grains (Fig. 2a vs. Fig. 3a,c). Zou et al. [44] affirmed that the recrystallization phenomenon occurred in the initial coarse columnar β-grains. In the same scenario, Huang et al. [45] showed that the equiaxed and half-equiaxed β-grains obtained after 1050 °C × 1 h followed by air cooling were formed by the splitting of the prior columnar β-grains due to their similar dimensions. Despite the same HT conditions, the equiaxed β-grains shown in this work (Fig. 3) are also characterized by coarsening phenomena due to a size increase of approximately +135% with respect to the prior columnar β-grains. This recrystallization phenomenon simultaneously promotes microstructural homogenization between the xz plane and the xy plane due to the polyhedric-shaped of equiaxed grains. The anisotropy in the mechanical behaviour, conferred

by the β-columnar grains in as-built and annealed samples, is consequently removed [46,47]. Therefore, direction of tensile load no longer influence the ductility, ultimate tensile and yield strength values of the recrystallized Ti6Al4V samples [1]. Argon cooling performed after solution heat treatment (Fig. 1b) promotes, first, α_GB formation at the equiaxed β-grain boundary and, second, a β → α+β transformation that is influenced by the thermal inertia of the build platform (Fig. 3b vs. Fig. 3d). Both microstructures show β-phase precipitation alongside the grain boundary of the α-phase due to the diffusion of β-stabilizer alloying elements. The α-phase generally nucleates from the α_GB and grows inside the equiaxed β-grain. The argon cooling, which is characterised by a slow cooling rate, promotes the nucleation of the α-phase directly connected to the α_GB (Fig. 3d), while higher one induces the nucleation of a fine α-phase on the grain boundary, on which the β-phase was formed (Fig. 3c). At the same time, the α_GB does not grow significantly (Fig. 3c) [35].

The vol% of the β-phase increases from 5.13 ± 0.13% in SHT samples to 6.16 ± 0.20% and 6.64 ± 0.19% in aged samples at 500 °C (Fig. 11) and 600 °C, respectively. This situation confirms the α′-martensite decomposition into the α+β phase during aging at 500 °C, similar to DTA and DSC analysis [1,42]. During the exposure at these temperatures, the diffusion of vanadium from the α′-martensite hcp lattice promotes the β-phase precipitation at the boundaries of the α′-martensite laths and their consequently transformation in α-phase. Coarsening phenomena of the same β-phase are instead obtained in aged samples at 600 °C, as listed in Table 4. As regards the obtained coarsening phenomena of the α-phase (Table 4), Gallaraga et al. [25] proposed the following equation to describe them:

$$\delta_{\alpha_{lath}} = \delta_{\alpha_{lath}(t=0)} \bullet t^{\left(\frac{T-850}{1000}\right)} \tag{1b}$$

where $\delta_{\alpha_{lath}}$ and $\delta_{\alpha_{lath}(t=0)}$ are the α-phase thicknesses before (t = 0) and after the HT, respectively, and t is the holding time at temperature T in hours and Kelvin, respectively. Eq. (1) underestimates the real value of the α-phase thickness in aged samples at 600 °C (Table 4) by approximately 20%.
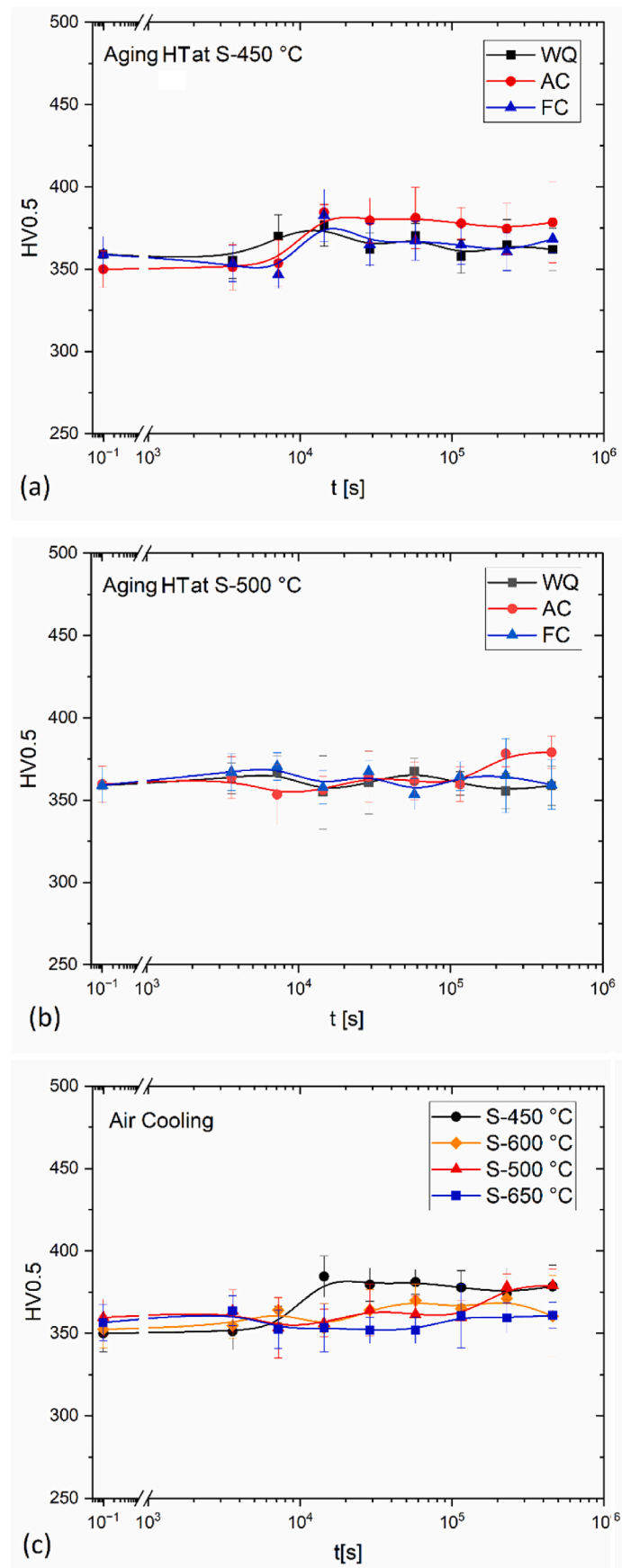
Fig. 8. Aging profiles obtained both at S-450 °C (a) and S-500 °C (b) where WQ, AC, and FC indicate water quenching, air cooling and furnace cooling, respectively. (c) Overlap of aging curves carried out after aging at S-450, S-500, S-600, and S-650 °C followed by AC.

Table 5
HV measurements of aged Ti6Al4V samples at 450 °C and followed by WQ, AC, and FC.

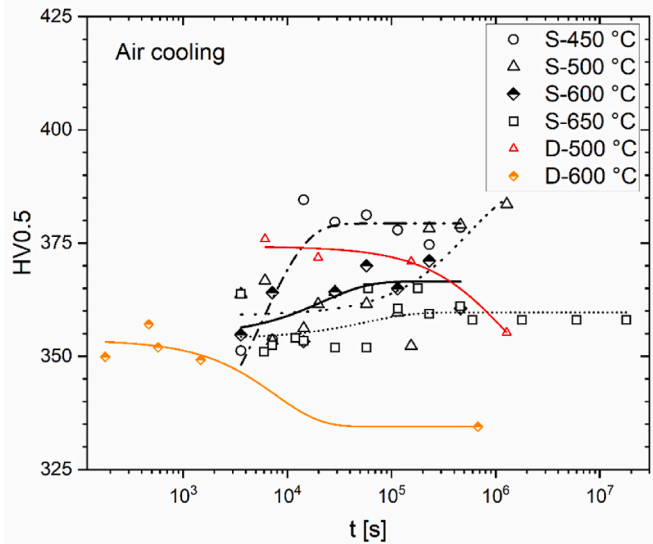|	WQ, [HV0.5]	AC, [HV0.5]	FC, [HV0.5]
Solubilized at 1050 °C	355 ± 12		
Peak-aging (4 h)	377 ± 10	385 ± 13	383 ± 12
128 h	362 ± 13	378 ± 20	368 ± 8

Fig. 9. HV measured in static (black lines) and dynamic (orange and red lines) conditions during the exposure at 450–600 °C and 500–600 °C, respectively. (For interpretation of the references to colour in this figure legend, the reader is referred to the Web version of this article.)
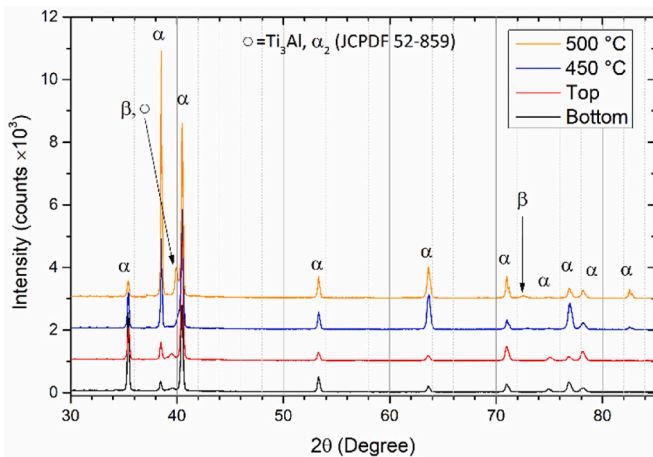

Fig. 10. Dimensions of α-phase, β-phase, and β-grain of the solubilized Ti6Al4V sample in Bottom and Top regions.

4.2. Vickers microhardness

The different as-built microstructural morphologies among the xz (Fig. 2a) and xy planes (Fig. 2b), in terms of both α′-laths and β-grains, promote a Vickers microhardness variation from (402 ± 10) HV0.5 on the xz plane to (385 ± 13) HV0.5 on the xy plane. The 5% HV variation is essentially conferred by the different α′-lath orientations with respect to the load axis of the Vickers indenter, as widely analyzed in Ref. [4] and reported in Ref. [37].

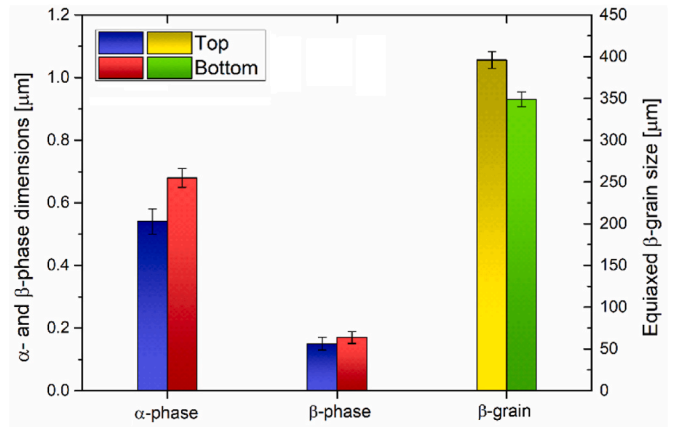After the recrystallization process occurred at 1050 °C and the

Fig. 11. XRD patterns of the solubilized (top and bottom regions) and aged Ti6Al4V samples at 450 °C and 500 °C followed by air cooling.

Table 6
Vickers microhardness of several morphologies of the α-phase into solubilized Ti6Al4V samples.

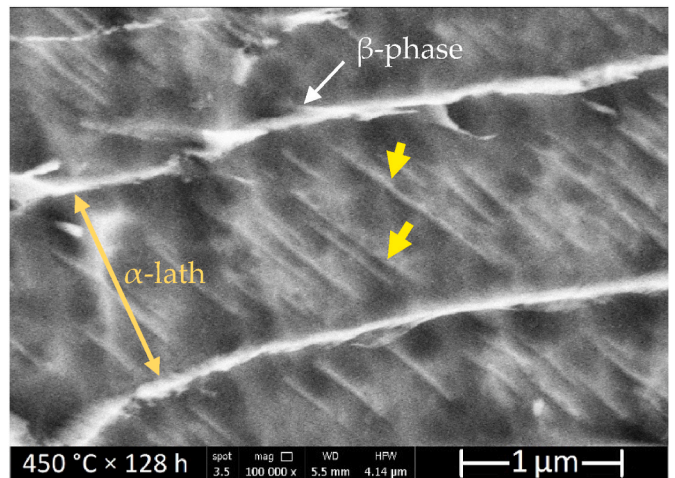| Morphology	α-phases				
	Fine colonies (Fig. 3d)	Coarse colonies (Fig. 3d)	Fine laths (Fig. 3b)	Coarse lath (Fig. 3b)	GB (Fig. 3b, d)
HV0.1	400 ± 10	360 ± 15	375 ± 6	358 ± 10	410 ± 15

Fig. 12. Micro- and nanostructures revealed into α-laths present in aged Ti6Al4V samples at 450 °C.

precipitation phenomena, the average HV values decrease up to (363 ± 15) HV0.5 and (363 ± 30) HV0.5 for the Top (Fig. 3a) and Bottom (Fig. 3c), respectively. Despite the microstructural variations observed in Figs. 3, Figs. 4 and 5, the comparability of HV values at the Top and Bottom is due to the balance between the α-phase and β-grain dimensions (Fig. 10). In fact, the Top region shows a smaller α-phase than the bottom region and martensite needles, which are contained in large β-grains. Therefore, the lower β-grain boundary amount in the Top region balances the higher contribution to HV conferred by both the small α-phase and the presence of martensite needles (Fig. 3a).

High error values associated with each HV0.5 measurement are conferred by the several morphologies of the α-phase and the presence of the α_GB (Figs. 3 and 5). Structures characterizing by different HV0.1 values, as listed in Table 6. For these reasons, the HV0.5 measurements
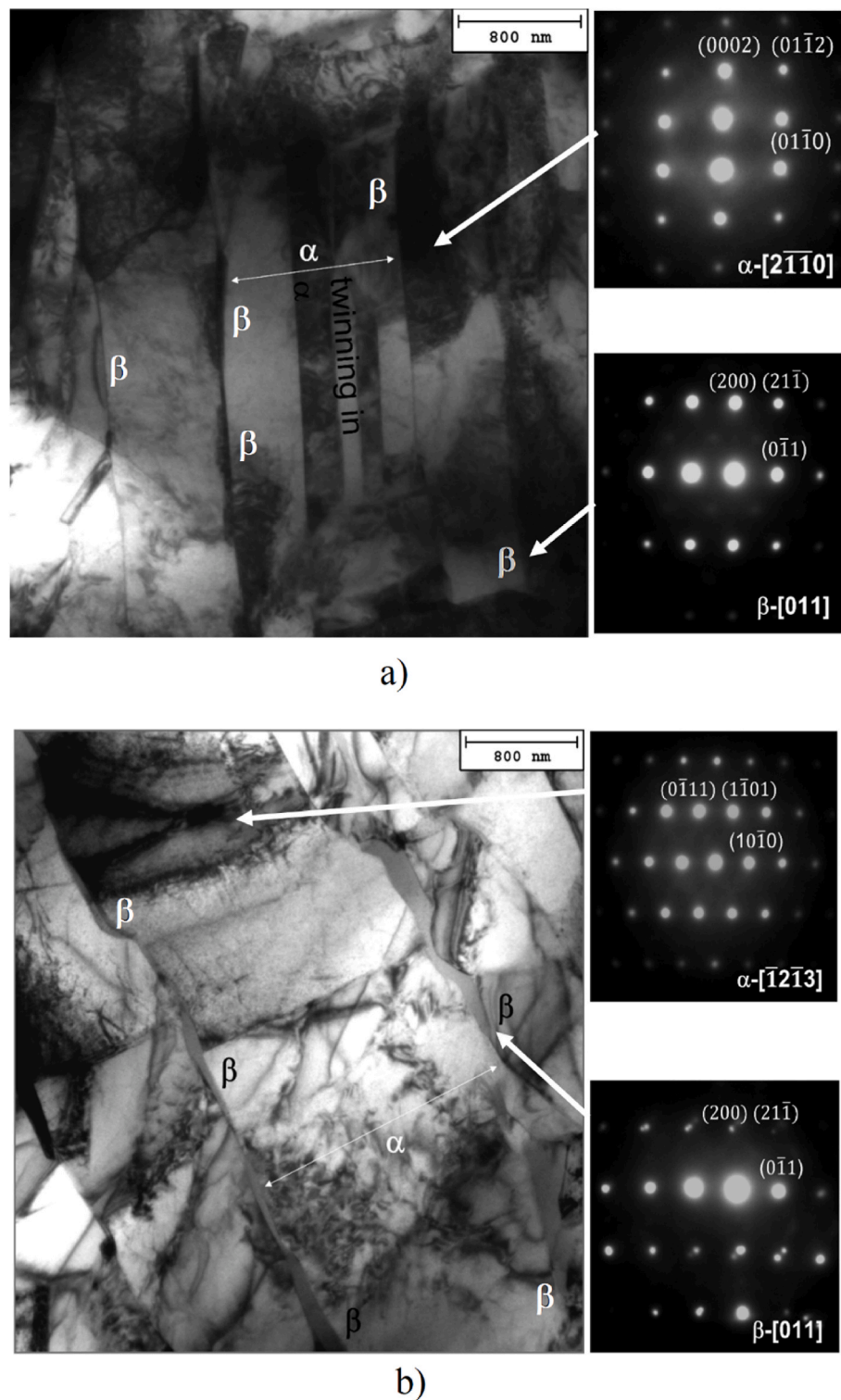
Fig. 13. TEM representative micrographs of the crept heat subjected to heating at 500 °C/h, where decomposition phenomena of α′-martensite into α+β phases is reported, a); sample crept and subjected to heating at 650 °C/h, showing the α-lath widening induced by the high temperature aging treatment, b).

of the Bottom region (Fig. 3c and d) of the SHT sample have an associated error higher than that of the Top region (Fig. 3a and b).

In the same scenario, another previously discussed Vickers measurements are also influenced by the Ti–Al binary precipitates, already found in the SHT microstructure (Figs. 5 and 6), as also reported in Ref. [22]. Precipitation phenomena of both Ti_3Al and $TiAl$ can first occur during the L-PBF process due to high heat inputs and Al segregation during rapid cooling [1,48]. At the same time, the precipitation

phenomena may also occur during the heating ramp used for the SHT at 1050 °C, thanks to the holding time of 2 h at the precipitation temperature range of 450–650 °C [26,49]. In this scenario, it is useful to emphasize that the dissolution temperatures of Ti_3Al and $TiAl$ precipitates are approximately 1100–1300 °C [50], so the SHT at 1050 °C cannot dissolve them. According to the Ti–Al binary phase diagram, the $TiAl_3$ phase (Fig. 6) can also precipitate into the as-built samples, and the following SHT at 1050 °C cannot dissolve it again [51,52]. The
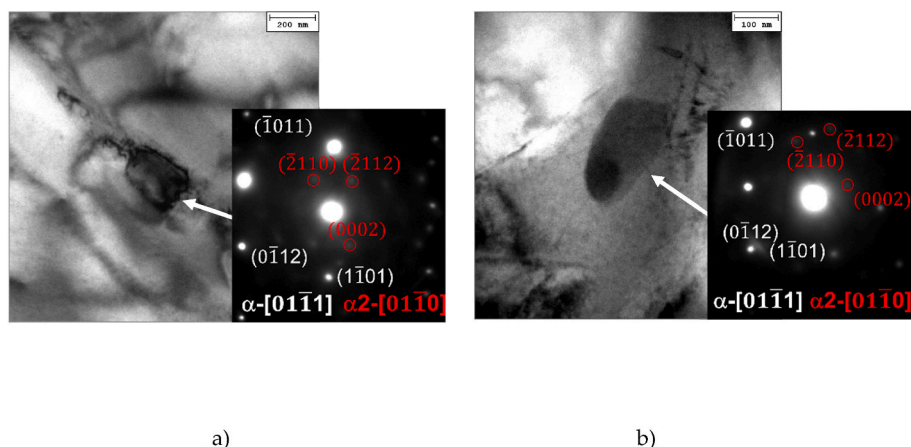
a)

b)

Fig. 14. TEM representative micrographs of the crept heat subjected to heating at 500 °C/h, a), and subjected to heating at 650 °C/h, b), showing the presence of Ti$_3$Al α$_2$ phase.
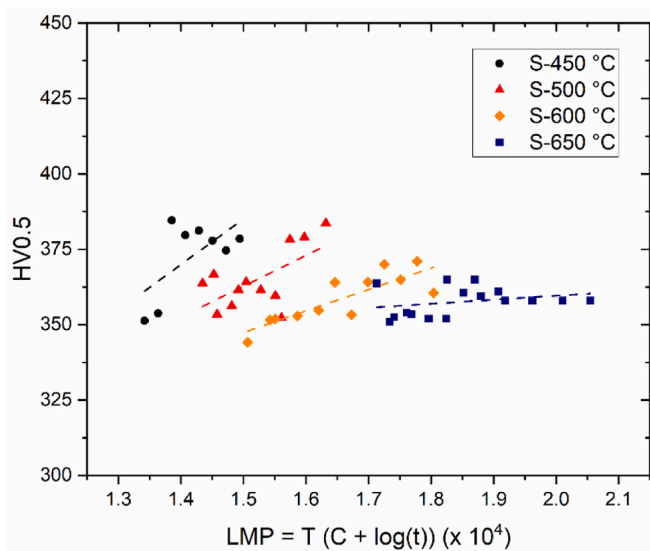

Fig. 15. Vickers microhardness versus Larson-Miller Parameter for aged Ti6Al4V samples at 450 °C, 500 °C, and 600 °C followed by air cooling.

following aging HTs continue to increase the precipitation phenomena of Ti–Al precipitates, as highlighted by both the XRD spectra in Fig. 11 and SEM micrographs in Fig. 5.

No microstructural variations are revealed in aged samples at 450 °C (Table 4), and the increase in HV measurements up to (377 ± 10) HV0.5 is conferred by the precipitation phenomena. At the same time, SEM observations revealed the presence of micro- and nanostructures in the α-lath (Fig. 12), which are absent in the SHT samples (Fig. 5) and less detectable with increasing aging temperature (i.e., 500 °C and 600 °C). Shan et al. [53] and Haubrick et al. [54] found the same structures in coarse α-laths and defined them as planar faults that can increase the HV microhardness. Defects hindering the movement of dislocations. On the other hand, Cao et al. [24] associate these micro- and nanostructures with twin structures, which are also observed in annealed samples at 800 °C × 2 h.

In contrast, samples aged at 500 °C do not show a real peak-aging condition considering the 5% HV variation obtained after 64 h (air cooling in Fig. 7b). The TEM micrographs of Fig. 13a show the occurrence of α′-martensite → α+β decomposition. The alloy microstructure was also characterized by an irrelevant presence of nanostructured phases within the α-lath, revealing a scarce precipitation phenomenon

induced by the alloy subjected to postproduction heat treatment at 500 °C.

The aging profiles highlight that the hardness contribution conferred by the precipitation phenomena, revealed through XRD and SEM observations, is balanced by both the α′-martensite → α+β decomposition and the lower presence of the micro- and nanostructures shown in Fig. 12. At 650 °C, TEM micrographs (Fig. 13b) clearly show a significant α-lath size increment induced by the high-temperature exposure of the alloy. At the same temperatures, TEM micrographs presented in Fig. 14a and b shows α$_2$-Ti$_3$Al precipitates into α-laths.

Finally, the similar trend between the aged samples at 600 °C and 500 °C suggests a substantial contribution promoted by the precipitation phenomena: the α-phase size increases by approximately 30%, and the HV values decrease as described by the well-known Hall-Petch equation [55]. It correlates the inverse-square of the average grain size, considered here as α-lath [4,45], to the yield strength (σ_y), which is strictly related to the Vickers microhardness [56]. In this scenario, the increment of the α-lath size from 0.63 μm to 0.94 μm (Table 4) should have promoted an HV reduction of approximately 12%. Similar results are shown in Refs. [1,4,57,58]. After the same high-temperature exposure, the alloy also shows a certain instability in the case of dynamic precipitation. Consequently, high temperatures cause a moderate variation in the properties of Ti6Al4V samples.

To correlate the effects of HT temperature and time on the obtained mechanical properties, Hollomon and Jaffe [59] proposed time–temperature correlations in tempering steels that relate the hardness (HV) to the tempering parameter P, also known as the Larson-Miller parameter (LMP), as follows:

$$P = T(C + \log(t)) \tag{2}$$

where T, t, and C are temperature [K], time [s], and a constant [−] that depends on the composition and state of the material. This constant is defined as follows:

$$C = -\log(t_0) = -\log\left[t \exp\left(-\frac{Q}{RT} \right) \right] \tag{3}$$

where t, Q, R and T are time [s], activation energy expressed in [$kJ\,mol^{-1}$], gas constant [$JK\,mol^{-1}$], and temperature [K]. According to Chao et al. [60], C is assumed to be equal to 15, and the obtained results from Eq. (2) were plotted with HV values for each investigated aging temperature (Fig. 15). The same graph shows that linear trends can describe the HV variations as a function of LMP. Linear trends showing faster increment of the Vickers microhardness with the lower aging temperatures thanks to the previously discussed microstructural variations (Section 4.1.).

5. Conclusions

The present paper aims to investigate static and dynamic precipitation phenomena that occurred in a laser-powder bed-fused Ti6Al4V alloy after SHT and aging at 450, 500, 600, and 650 °C. The main findings can be drawn as follows:

- The microstructures of the Top and Bottom sample zones show α-laths and α-colonies arranged in a Widmanstätten structure, respectively. Despite this morphological variation, the HV values remain constant at 363 HV0.5.
- Aging heat treatment at 500 °C promotes an increase in the vol% of the β-phase due to α′-martensite decomposition, while coarsening phenomena (+ 50%) of α-phase laths were achieved after exposure at 600 °C.
- The presence of α-Ti$_3$Al precipitates was relieved after the laser-powder bed fusion process, but their density increased with aging heat treatment temperature (450, 500 °C).
- The Ti6Al4V alloy generally showed a certain instability during the analyzed aging conditions, which caused a moderate variation in its properties. At 450 °C, peak-aging conditions were reached only after 4 h of exposure. Due to the martensite decomposition and the lower presence of stacking faults, aging at 500 °C promoted the peak-aging conditions at 64 h of exposure. At the same temperature, they were anticipated at 1 h due to the dynamic precipitation phenomena. Higher temperatures did not show evident peak-aging conditions in either static or dynamic precipitation phenomena.

CRediT authorship contribution statement

Emanuela Cerri: Conceptualization, Methodology, Validation, Writing – original draft, Writing – review & editing, Visualization, Supervision, Project administration, Funding acquisition. **Emanuele Ghio:** Conceptualization, Methodology, Validation, Investigation, Writing – original draft, Writing – review & editing, Visualization, Project administration. **Stefano Spigarelli:** Investigation, Data curation. **Marcello Cabibbo:** Investigation, Data curation, Writing – original draft. **Giovanni Bolelli:** Investigation, Data curation, Writing – original draft, Writing – review & editing.

Declaration of competing interest

The authors declare that they have no known competing financial interests or personal relationships that could have appeared to influence the work reported in this paper.

Data availability

No data was used for the research described in the article.

References

[1] E. Ghio, E. Cerri, Additive Manufacturing of AlSi10Mg and Ti6Al4V Lightweight alloys via laser powder bed fusion: a review of heat treatments effects, Materials 15 (6) (2022), https://doi.org/10.3390/ma15032047, 2047.
[2] P. Bocchetta, L.-Y. Chen, J. Tardelli, A. dos Reis, F. Almeraya-Calderón, P. Leo, Passive layers and corrosion resistance of biomedical Ti-6Al-4V and β-Ti alloys, Coatings 11 (5) (2021) 478, https://doi.org/10.3390/coatings11050487.
[3] F. Chen, Y. Gu, G. Xu, Y. Cui, H. Chang, L. Zhou, Improved fracture toughness by microalloying of Fe in Ti-6Al-4V, Mater. Des. 185 (2020), 108251, https://doi.org/10.1016/j.matdes.2019.108251.
[4] E. Cerri, E. Ghio, G. Bolelli, Effect of surface roughness and industrial heat treatments on the microstructure and mechanical properties of Ti6Al4V alloy manufactured by laser powder bed fusion in different built orientations, Mater. Sci. Eng. 851 (2022), 143635, https://doi.org/10.1016/j.msea.2022.143635.
[5] H. Bai, H. Deng, L. Chen, X. Liu, X. Qin, D. Zhang, T. Liu, X. Cui, Effect of heat treatment on the microstructure and mechanical properties of selective laser-melted Ti64 and Ti-5Al-5Mo-5V-1Cr-1Fe, Metals 11 (2021) 534–545, https://doi.org/10.3390/met11040534.
[6] G. Haar, T. Becker, Selective laser melting produced Ti-6Al-4V: post-process heat treatments to achieve superior tensile properties, Materials 11 (2018) 146, https://doi.org/10.3390/ma11010146.
[7] D. Kent, G. Wang, W. Wang, M. Dargusch, Influence of ageing temperature and heating rate on the properties and microstructure of β Ti alloy, Ti–6Cr–5Mo–5V–4Al, Mater. Sci. Eng. 531 (2012) 98–106, https://doi.org/10.1016/j.msea.2011.10.040.
[8] J. Yang, H. Yu, J. Yin, M. Gao, Z. Wang, X. Zeng, Formation and control of martensite in Ti-6Al-4V alloy produced by selective laser melting, Mater. Des. 108 (2016) 308–318, https://doi.org/10.1016/j.matdes.2016.06.117.
[9] A. Antonysamy, J. Meyer, P. Prangnell, Effect of build geometry on the -grains structure and texture in additive manufacture of Ti-6Al-4V by selective electrons beam melting, Mater. Char. 84 (2013) 153–168, https://doi.org/10.1016/j.matchar.2013.07.012.
[10] S. Liu, Y. Shin, Additive manufacturing of Ti6Al4V alloy: a review, Mater. Des. 164 (2019), 107552, https://doi.org/10.1016/j.matdes.2018.107552.
[11] P. Lekoadi, M. Tlotleng, K. Annan, N. Maledi, B. Masina, Evaluation of heat treatment parameters on microstructure and hardness properties of high-speed Selective Laser Melted Ti6Al4V, Metals 11 (2021) 255–270, https://doi.org/10.3390/met11020255.
[12] L. Thijs, F. Verhaeghe, T. Craeghs, J. Humbeeck, J. Kruth, A study of the microstructural evolution during selective laser manufacturing of Ti-6Al-4V, Acta Mater. 58 (2010) 3303–3312, https://doi.org/10.1016/j.actamat.2010.02.004.
[13] S.Q. Wu, Y.J. Lu, Y.L. Gan, T.T. Huang, C.Q. Zhao, J.J. Lin, S. Guo, J.X. Lin, Microstructural evolution and microhardness of a selective-laser-melted Ti–6Al–4V alloy after post heat treatments, J. Alloys Compd. 672 (2016) 643–652, https://doi.org/10.1016/j.jallcom.2016.02.183.
[14] P. Barriobero-Vila, J. Gussone, J. Haubrich, S. Sandlöbes, J.C. Da Silva, P. Cloentes, N. Schell, G. Requena, Inducing stable α + β microstructures during selective laser melting of Ti-6Al-4V using intensified intrinsic heat treatments, Materials 10 (3) (2017) 268, https://doi.org/10.3390/ma10030268.
[15] M. Chávez-Díaz, M. Escudero-Rincón, E. Arce-Estrada, R. Cabrera-Sierra, Effect of the heat-treated Ti6Al4V alloy on the fibroblastic cell response, Materials 11 (1) (2018) 21, https://doi.org/10.3390/ma11010021.
[16] H. Ali, L. Ma, H. Ghadbeigi, K. Mumtaz, In-situ residual stress reduction, martensitic decomposition and mechanical properties enhancement through high temperature powder bed pre-heating of selective laser melted Ti6Al4V, Mater. Sci. Eng. 695 (2017) 211–220, https://doi.org/10.1016/j.msea.2017.04.033.
[17] Z. Song, X. Zeng, L. Wang, Laser additive manufacturing of titanium alloys with various Al contents, Mater. Res. Lett. 11 (2023) 391–398, https://doi.org/10.1080/21663831.2023.2165418.
[18] Z. Wu, C. Qiu, V. Venkatesh, H. Fraser, R. Williams, G. Viswanathan, M. Thomas, S. Neg, R. Banerjee, M. Loretto, The influence of precipitation of α$_2$ on properties and microstructure in TIMETAL 6-4, Metall. Mater. Trans. 44 (2013) 1706–1713, https://doi.org/10.1007/s11661-012-1530-9.
[19] N. Ramachandiran, H. Asgari, F. Dibia, R. Eybel, A. Gerlich, E. Toyserkani, Effect of non-lamellar α precipitate morphology on the mechanical properties of Ti5553 parts made by laser powder-bed fusion at high laser scan speeds, Mater. Sci. Eng. 841 (2022), 143039, https://doi.org/10.1016/j.msea.2022.143039.
[20] H. Ali, H. Ghadbeigi, K. Mumtaz, Effect of scanning strategies on residual stress and mechanical properties of Selective Laser Melted Ti6Al4V, Mater. Sci. Eng. 712 (2018) 175–187, https://doi.org/10.1016/j.msea.2017.11.103.
[21] F. Kaschel, R. Vijayaraghavan, A. Shmeliov, E. McCarthy, M. Canavan, P. McNally, D. Dowling, V. Nicolosi, M. Celikin, Mechanism of stress relaxtion and phase transformation in additively manufactured Ti-6Al-4V via in-situ high temperature XRD and TEM analyses, Acta Mater. 188 (2020) 720–732, https://doi.org/10.1016/j.actamat.2020.02.056.
[22] S. Spigarelli, C. Paoletti, E. Cerri, E. Santecchia, M. Cabibbo, Creep resposne of Ti-6Al-4V alloy produced by additive manufacturing: effect of annealing at 1050 °C, Mater. Sci. Eng. 860 (2022), 144278, https://doi.org/10.1016/j.msea.2022.144278.
[23] W. Xu, M. Brandt, S. Sun, E. J, Q. Liu, K. Latham, K. Xia, M. Qian, Additive manufacturing of strong and ductile Ti-6Al-4V by selective laser melting via in situ martensite decomposition, Acta Mater. 85 (2015) 74–84, https://doi.org/10.1016/j.actamat.2014.11.028.
[24] S. Cao, R. Chu, X. Zhou, K. Yang, Q. Jia, C.S. Lim, A. Huang, X. Wu, Role of martesnite decomposition in tensile properties of selective laser melted Ti-6Al-4V, J. Alloys Compd. 744 (2018) 357–363, https://doi.org/10.1016/j.jallcomp.2018.02.111.
[25] H. Gallaraga, D. Lados, R. Dehoff, M. Kirka, P. Nandwana, Effect of the microstructure and porosity of Ti-6Al-4V ELI alloy fabricated by electron beam melting (EBM), Addit. Manuf. 10 (2016) 47–57, https://doi.org/10.1016/j.addma.2016.02.003.
[26] S. Zhang, X. Lin, J. Chen, W. Huang, Heat-treated microstructure and mechanical properties of laser solid forming Ti-6Al-4V alloy, Rare Met. 28 (2009) 537, https://doi.org/10.1007/d12598-009-0104-5.

[27] G. Kasperovich, J. Hausmann, Improvement of fatigue resistance and ductility of Ti6Al4V processed by selective laser melting, J. Mater. Process. Technol. 220 (2015) 202–214, https://doi.org/10.1016/j.jmatprotec.2015.01.025.

[28] Z. Wang, S. Yang, X. Peng, Z. Gao, Effects of defects in laser selective melting of Ti-6Al-4V alloy on microstructure and mechanical properties after heat treatment, Opt Laser. Technol. 156 (2022), 108522, https://doi.org/10.1016/j.optlastec.2022.108522.

[29] E. Cerri, E. Ghio, G. Bolelli, Ti6Al4V-ELI alloy manufactured via laser powder-bed fusion and heat-treated below and above the β-transus: effects of sample thickness and sandblasting post-process, Appl. Sci. 11 (12) (2022) 5359, https://doi.org/10.3390/app12115359.

[30] J. Tiley, T. Searles, E. Lee, S. Kar, R. Banerjee, J. Russ, H. Fraser, Quantification of microstructural features in α/β titanium alloys, Mater. Sci. Eng. 372 (2004) 191–198, https://doi.org/10.1016/j.msea.2003.12.008.

[31] X. Li, L. Cui, J. Li, Y. Chen, W. Han, S. Shonkwiler, S. McMains, Automation of intercept method for grain size measurement: a topological skeleton approach, Mater. Des. 224 (2022), 111358, https://doi.org/10.1016/j.matdes.2022.111358.

[32] M. Pantawane, Y. Ho, S. Joshi, N. Dahotre, Computational assessment of thermokinetics and associated microstructural evolution in laser powder bed fusion manufacturing of Ti6Al4V alloy, Sci. Rep. 10 (2020) 7579–7593, https://www.nature.com/articles/s41598-020-63281-4.

[33] Y. Huang, T. Fleming, S. Clarck, S. Marussi, K. Fezzaa, J. Thiyagalingam, C. Leung, P. Lee, Keyhole fluctuation and pore formation mechanisms during laser powder bed fusion additive manufacturing, Nat. Commun. 13 (2022) 1170, https://doi.org/10.1038/s41467-022-28694-x.

[34] T. Ahmed, H. Rack, Phase transformation during cooling in α+β titanium alloys, Mater. Sci. Eng. 243 (1) (1998) 206–211, https://doi.org/10.1016/S0921-5093(97)00802-2.

[35] H. Yi, J. Kim, Y. Kim, S. Shin, Effects of cooling rate on the microstructure and tensile properties of wire-arc additive manufactured Ti–6Al–4V alloy, Met. Mater. Int. 26 (2020) 1235–1246, https://doi.org/10.1007/s12540-019-00563-1.

[36] M. Motyka, Martensite Formation and decomposition during traditional and AM processing of two-phase titanium alloys—an overview, Metals 11 (3) (2021) 481, https://doi.org/10.3390/met11030481.

[37] J. Keist, T. Palmer, Development of strength-hardness relationships in additively manufactured titanium alloys, Mater. Sci. Eng. 693 (2017) 214–224, https://doi.org/10.1016/j.msea.2017.03.102.

[38] J. Akram, D. Pal, B. Stucker, Establishing flow stress and elongation relationshops as a function of microstrucutral features of Ti6Al4V alloy processed using SLM, Design 3 (2019) 21, https://doi.org/10.3390/designs3020021.

[39] J. Rousseau, A. Bois-Brochu, C. Blais, Effect of oxygen content in new and reused powder on microstructural and mechanical properties of Ti6Al4V parts produced by directed energy deposition, Addit. Manuf. 23 (2018) 197–205, https://doi.org/10.1016/j.addma.2018.08.011.

[40] J. Sieniawski, W. Ziaja, K. Kubiak, M. Motyka, Microstructure and mechanical properties of high strength two-phase titanium alloys, Adv. Prop. Control (2013) 69–80, https://doi.org/10.5772/56197.

[41] R. Ma, Z. Liu, W. Wang, G. Xu, W. Wang, Microstructures and mechanical properties of Ti6Al4V-Ti48Al2Cr2Nb alloys fabricated by laser melting deposition of powder mixtures, Mater. Char. 164 (2020), 110321, https://doi.org/10.1016/j.matchar.2020.110321.

[42] Y. Vahidshad, A. Khodabakhshi, Effect of solution treatment and aging temperature on α′ and Ti₃Al(α₂) phase formation and mechanical properties of water-quenched Ti–6Al–4V, Metall. Micr. Anal. 11 (2022) 59–71, https://doi.org/10.1007/s13632-021-00818-7.

[43] Y. Watanabe, M. Sato, T. Chiba, H. Sato, N. Sato, S. Nakano, 3D visualization of top surface structure and pores of 3D printed Ti-6Al-4V samples manufactured with TiC heterogeneous nucleation site particles, Metall. Mater. Trans. 51 (2020) 1345–1352, https://doi.org/10.1007/s11661-019-05597-z.

[44] Z. Zou, M. Simonelli, J. Katrib, G. Dimitrakis, R. Hauge, Refinement of the grain structure of additive manufactured titanium alloys via epitaxial recrystallization enabled by rapid heat treatment, Scripta Mater. 180 (2020) 66–70, https://doi.org/10.1016/j.scriptamat.2020.01.027.

[45] Q. Huang, X. Liu, X. Yang, R. Zhang, Z. Shen, Q. Feng, Specific heat treatment of selective laser melted Ti-6Al-4V for biomedical applications, Front. Mater. Sci. 9 (2015) 373–381, https://doi.org/10.1007/s11706-015-0315-7.

[46] Z. Zou, M. Simonelli, J. Kabrit, G. Dimitrakis, R. Hague, Microstructure and tensile properties of additive manufactured Ti-6Al-4V with refined prior-β grain structure obtained by rapid heat treatment, Mater. Sci. Eng. 814 (2021), 141271, https://doi.org/10.1016/j.msea.2021.141271.

[47] Z. Zheng, X. Jin, Y. Bai, Y. Yang, C. Ni, W.F. Lu, H. Wang, Microstructure and anisotropic mechanical properties of selective laser melted Ti6Al4V alloy under different scanning strategies, Mater. Sci. Eng. 831 (2022), 142236, https://doi.org/10.1016/j.msea.2021.142236.

[48] W. Abd-Elaziem, S. Elkatatny, A.-E. Abd-Elaziem, M. Khedr, M. El-baky, M. Hassan, M. Abu-Okaif, M. Mohammed, A. Järvenpää, T. Allam, A. Hamada, On the current research progress of metallic materials fabricated by laser powder bed fusion process: a review, J. Mater. Res. Technol. 20 (2022) 681–707, https://doi.org/10.1016/j.jmrt.2022.07.085.

[49] E. Jimenez, A. Kreitcberg, E. Moquin, V. Brailovski, Influence of post-processing conditions on the microstructure, static, and fatigue resistance of laser powder bed fused Ti-6Al-4V components, Manuf. Mater. Process. 6 (4) (2022) 85, https://doi.org/10.3390/jmmp6040085.

[50] B. Distl, K. Hauschildt, F. Pyczak, F. Stein, Phase equilibria in the Ti-rich part of the Ti-Al-Nb system—Part II: high-temperature phase equilibria between 1000 and 1300 °C, J. Phase Equilibria Diffus. 43 (2022) 554–575, https://doi.org/10.1007/s11669-022-00999-w.

[51] T. Tian, J. Shen, S. Hu, J. Gou, E. Kannatey-Asibu, Wire and arc additive manufactured Ti–6Al–4V/Al–6.25Cu dissimilar alloys by CMT-welding: effect of deposition order on reaction layer, Sci. Technol. Weld. Join. 25 (2020) 73–80, https://doi.org/10.1080/13621718.2019.1629379.

[52] J. Schuster, M. Palm, Reassessment of the binary Aluminum-Titanium phase diagram, J. Phase Equilibria Diffus. 27 (2006) 255–277, https://doi.org/10.1361/154770306X109809.

[53] D. Shan, Y. Zong, T. Lu, Y. Lv, Microstructural evolution and formation mechanism of FCC titanium hydride in Ti–6Al–4V–xH alloys, J. All. Compd. 427 (2007) 229–234, https://doi.org/10.1016/j.jallcom.2006.02.058.

[54] J. Haubric, J. Gussone, P. Barriero-Villa, P. Kürnsteiner, E. Jägle, D. Raabe, N. Schell, G. Requena, The role of lattice defects, element partitioning and intrinsic heat effects on the microstructure in selective laser melted Ti-6Al-4V, Acta Mater. 167 (2019) 136–148, https://doi.org/10.1016/j.actamat.2019.01.039.

[55] R. Armstrong, Engineering science aspects of the Hall–Petch relation, Acta Mech. 225 (2014) 1013–1028, https://doi.org/10.1007/s00707-013-1048-2.

[56] J. Cahoon, W. Broughto, A. Kutzak, Determination of yield strength from hardness measurements, Metall. Transaction. 2 (7) (1971) 1979–1983, https://doi.org/10.1007/BF02913433.

[57] B. Vrancken, L. Thjis, J. Kruth, J. Humbeeck, Heat treatments of Ti6Al4V produced by selective laser melting: microstructure and mechanical properties, J. Alloys Compd. 541 (2012) 177–185, https://doi.org/10.1016/j.jallcom.2012.07.022.

[58] P. Wanjara, D. Backman, F. Sikan, J. Gholipour, R. Amos, P. Patnaik, M. Brochu, Microstructure and mechanical properties of Ti-6Al-4V additively manufactured by electron beam melting with 3D Part Nesting and powder reuse influences, J. Manuf. Mater. Process. 6 (1) (2022) 21, https://doi.org/10.3390/jmmp6010021.

[59] J. Hollomon, L. Jaffe, Time-temperature relations in tempering steel, » Trans. AIME 162 (1945) 223–249.

[60] Q. Chao, P. Hodgson, H. Beladi, Thermal stability of an ultrafine grained Ti-6Al-4V alloy during post-deformation annealing, Mater. Sci. Eng. 694 (2017) 13–23, https://doi.org/10.1016/j.msea.2017.03.082.